

Article

Not peer-reviewed version

Corrosion Characteristics and Strength Degradation Mechanism of Metro Steel Fiber Reinforced Cementitious Materials under the Low-Carbon Target

Zhiqiang Yuan , Zhaojun Chen , Liming Yang , Bo Liu , [Minghui Liu](#) , [Yurong Zhang](#) *

Posted Date: 29 July 2025

doi: 10.20944/preprints202507.2412.v1

Keywords: steel fiber; stray current; Chloride ions; strength degradation mechanisms; X-CT



Preprints.org is a free multidisciplinary platform providing preprint service that is dedicated to making early versions of research outputs permanently available and citable. Preprints posted at Preprints.org appear in Web of Science, Crossref, Google Scholar, Scilit, Europe PMC.

Copyright: This open access article is published under a Creative Commons CC BY 4.0 license, which permit the free download, distribution, and reuse, provided that the author and preprint are cited in any reuse.

Article

Corrosion Characteristics and Strength Degradation Mechanism of Metro Steel Fiber Reinforced Cementitious Materials under the Low-Carbon Target

Zhiqiang Yuan ¹, Zhaojun Chen ¹, Liming Yang ¹, Bo Liu ¹, Minghui Liu ² and Yurong Zhang ^{3,4,*}

¹ China Construction Railway Investment South China CO., Ltd., Guangzhou 510663, China

² School of Civil Engineering, Beijing Jiaotong University, Beijing 100044, China

³ College of Civil Engineering, Zhejiang University of Technology, Hangzhou, 310014, China

⁴ Key Laboratory of Civil Engineering Structure & Disaster Prevention and Mitigation Technology of Zhejiang Province, Hangzhou, 310014, PR China

* Correspondence: yrzhang@zjut.edu.cn

Abstract

In the context of sustainable development, improving the durability of engineering materials and the service life of engineering projects is an important path to address engineering sustainability and low-carbon development. This study addresses the durability issues of steel fiber reinforced cementitious materials (SFRCM) under the combined action of stray current and chloride ions in metro engineering. Through simulated stray current-accelerated corrosion tests, combined with compressive strength tests and X-ray computed tomography (X-CT) analysis, the effects of steel fiber volume content (0.5%, 1.0%, 1.5%) and electrification duration (0–72 h) on the mechanical properties and corrosion mechanisms were systematically investigated. The results indicate that steel fiber content significantly influences corrosion rate and strength degradation. Specimens with 1.5% fiber content exhibited the highest initial compressive strength (58.43 MPa), but suffered a severe strength loss rate of 37.67% after 72 h of electrification. In contrast, specimens with 1.0% fiber content demonstrated balanced performance, achieving both high initial strength and superior corrosion resistance (19.66% strength loss after 72 h). X-CT analysis revealed that corrosion products initially filled pores during early stages but later induced microcracks in the matrix. Higher fiber content specimens exhibited increased large-pore ratios due to fiber agglomeration, accelerating chloride ion penetration. Furthermore, digital volume correlation (DVC) analysis demonstrated that steel fibers effectively dispersed loads and reduced stress concentration. However, post-corrosion fiber volume loss weakened their crack resistance capacity, highlighting the critical role of fiber integrity in structural durability.

Keywords: steel fiber; stray current; Chloride ions; strength degradation mechanisms; X-CT

1. Introduction

Driven by global low-carbon development goals and China's "Carbon Peak& Carbon Neutrality" strategy, urban rail transit, as the core carrier of the green transportation system, is embracing a historic development opportunity. Coastal cities, leveraging their economic vitality and population density, have significantly accelerated the construction of subway networks. Compared with traditional public transportation systems, the subway has become a key infrastructure for practicing urban transportation emission reduction due to its remarkable low-carbon advantages, such as fast operation speed, low energy consumption per unit of passenger and freight volume, and strong transportation capacity. Data shows that the carbon emission intensity of subway systems per

10,000 passenger trips can be reduced by more than 80% compared with private car travel, which is highly consistent with the goals of large-scale construction and low-carbon development. However, the sustainability of subway projects faces severe challenges. In the track power supply system, the stray current leakage problem of the rail as the return conductor forms a synergistic erosion effect with the high chloride underground environment. The coupling of electrochemical corrosion caused by stray current and corrosion induced by chloride ions leads to the rapid deterioration of the durability of traditional reinforced concrete structures [1].

To address the longevity requirements of materials in low-carbon construction, steel fiber-reinforced cementitious composites (SFRC)-a new type of tough material-have been applied in pilot projects such as Xi'an metro tunnels, Nanjing metro stations, and Guangzhou metro track slabs. The randomly distributed steel fibers improve the mechanical properties of concrete, theoretically reducing steel reinforcement usage and enhancing crack resistance, which aligns with the "material saving and carbon reduction" development direction of low-carbon building materials [2]. Current research focuses on the corrosion mechanism of reinforced concrete in stray current-chloride ion coupled environments, while durability studies on SFRC remain in their infancy. Carlos et al.[3] indicated that the corrosion depth of SFRC is typically less than 10 mm, demonstrating better durability than ordinary reinforced concrete, but failed to reveal its micro-damage mechanism. Long-term observations in industrial wastewater and coastal environments show that matrix rust expansion cracking caused by steel fiber corrosion is the main cause of material durability degradation [4]. However, existing studies mostly remain at the macro-mechanical property characterization level, lacking quantitative analysis of micro-damage during steel fiber corrosion. Specifically, under the low-carbon goal, the corrosion behavior of SFRC not only affects the service life of structures but also is closely related to the whole-life cycle carbon emissions of materials, corrosion-induced maintenance and reinforcement will significantly increase the project's life cycle carbon footprint.


Therefore, this paper takes the SFRC applied in a station project of Guangzhou Metro's Fangbai Intercity Railway as a case study. By integrating stray current accelerated corrosion tests with X-CT 3D imaging technology, it conducts a systematic investigation into the corrosion evolution process of concretes with varying steel fiber contents (0%, 0.5%, 1.0%, 1.5%) in chloride environment. The study focuses on analyzing how steel fiber content influences current transmission characteristics, pore structure evolution, and strength degradation regulation. From macro-to-micro scales, it reveals the corrosion damage mechanism of SFRC under the coupled action of stray current and chloride penetration, providing theoretical support and technical pathways for low-carbon-oriented material design and durability optimization in metro engineering.

2. Experimental Methods

2.1. Specimen Fabrication

Since coarse aggregates exhibit chemical inertness and typically do not participate in corrosion-related electrochemical reactions, mortar without coarse aggregates, comprising solely cement, water, and fine aggregates, can achieve better uniformity during casting. Thus, this study uses steel fiber-reinforced mortar (SFRM) instead of concrete to investigate the corrosion behavior of steel fibers. The cementitious material is PO 42.5 Portland cement, with a dosage of 530 kg/m³; the fine aggregate is standard sand with a maximum particle size of 1.0 mm, at a dosage of 1500 kg/m³; and the water-cement ratio is 0.5. Shear-type steel fibers with hooked ends are employed, and their key parameters are listed in Table 1.

Table 1. Main Parameters of Steel Fibers.

Shape	Tensile strength f_u / MPa	Length l_f / mm	Diameter d_e / mm	Aspect ratio l_f/d_e	Elastic l_f modulus E / GPa	density $\rho/(kg/m^3)$
	1250	35	0.55	65	200	7850

To meet the specimen size requirements for subsequent CT tests, cubic specimens with dimensions of 70.7 mm × 70.7 mm × 70.7 mm were designed. As the volume fraction of steel fibers increases, the mechanical properties of the material improve significantly. However, when the fiber content exceeds a critical threshold (typically 2.0%), fiber agglomeration tends to occur, compromising material homogeneity. Additionally, the degree of performance degradation due to fiber corrosion is closely related to the initial fiber content [5]. Considering these factors, three steel fiber volume fractions (0.5%, 1.0%, and 1.5%) were selected to investigate their effects on material properties.

Before specimen preparation, all molds were coated with oil. The mixed slurry was then poured into the molds, covered immediately to prevent moisture evaporation, and allowed to cure for 48 hours. During mixing, steel fibers were dispersed uniformly into the slurry to avoid agglomeration, which could affect test results. Finally, the specimens were demolded and cured in a water tank for 28 days.

This paper conducted tests and analyses on 36 specimens designed with 3 (steel fiber volume fraction) × 4 (stray current duration) × 3 (control variable samples) factorial arrangement, supplemented by a control specimen without steel fibers and unexposed to stray current, totaling 39 specimens in all. The specimens were labeled in the format Tx-y (as shown in Table 2), where T1-1.0 denotes the specimen subjected to 24 hours of stray current exposure with a steel fiber volume fraction of 1.0%.

Table 2. Test Parameters.

No.	Fiber Dosage /(kg/m ³)	Energization time/ h	No.	Fiber Dosage /(kg/m ³)	Energization time/ h
T0-0.5%	39.3	0	T2-1.0%	78.6	48
T1-0.5%	39.3	24	T3-1.0%	78.6	72
T2-0.5%	39.3	48	T0-1.5%	117.9	0
T3-0.5%	39.3	72	T1-1.5%	117.9	24
T0-1.0%	78.6	0	T2-1.5%	117.9	48
T1-1.0%	78.6	24	T3-1.5%	117.9	72

2.2. Stray Current Energization Method

Potentiostatic method was employed to simulate the stray current environment, with the test voltage set at 30 V to ensure comparability between test conditions and actual engineering scenarios. A 3.5% NaCl solution was used to mimic chloride penetration. Prior to energization, specimens were immersed in the NaCl solution for 48 hours, followed by the initiation of current application. To maintain test condition stability, the electrolyte solution was replaced every 24 hours for specimens with prolonged energization cycles, ensuring constant ionic concentration. Additionally, control

group tests were designed to explore the isolated effect of stray current on the corrosion process: specimens after standard curing were immersed in 3.5% sodium chloride solution to simulate natural corrosion environment without current interference.

2.3. Compressive Strength Test

Three cubic specimens were set as parallel groups for each test set to conduct compressive strength tests, using a 3000 kN microcomputer-controlled pressure testing machine with a loading rate of 5 kN/s. The material strength loss rate K_c was adopted as the key parameter to quantitatively evaluate the material's resistance to stray current corrosion, with the expression defined as Equation (1):

$$K_c = \frac{f_c(T_0) - f_c(T_i)}{f_c(T_0)} \times 100\% \quad (1)$$

where $f_c(T_0)$ is the compressive strength of the specimen at time T_0 , and $f_c(T_i)$ is the compressive strength after energization for time T_i .

2.4. X-CT Test

A 320 kV X-ray computed tomography (CT) in-situ tester was used for X-CT scanning, with the instrument's gray value range spanning 0 to 64000. The CT layers were 16-bit images, and upon completion of scanning, each group yielded 2000 slices with a resolution of 2000×2000 pixels. The CT images were accurately segmented using a gray value based threshold segmentation method [6], where higher material density corresponds to a larger gray value. The gray values of each phase in the sample are ordered from smallest to largest as: pores, mortar, corrosion products, and steel fibers.

Mathematical morphology was applied to quantify the reconstructed images after segmentation. The volume of the target material was calculated as follows:

$$V_{XCT} = N_{VOX} \times Z_{VOX} \quad (2)$$

where V_{XCT} is the spatial volume of the target material in mm^3 , N_{VOX} is the number of spatial voxels of the target material, and Z_{VOX} is the spatial voxel size in mm^3 .

The volume loss rate η_i of the target material at time T_i is expressed as:

$$\eta_i = \frac{V(T_0) - V(T_i)}{V(T_0)} \times 100\% \quad (3)$$

where $V(T_0)$ is the volume of the target material at time T_0 (i.e., the volume before stray current energization), and $V(T_i)$ is the volume of the target material at time T_i .

2.5. Digital Volume Correlation (DVC) Technique

DVC technique calculates the positional changes of each voxel in an object under different time or loading conditions by comparing 3D images at distinct moments, enabling the acquisition of internal deformation and strain information [6]. The specific procedures for DVC analysis are as follows: First, the same sample with varying corrosion degrees was sequentially scanned by X-CT to obtain 3D volume data at 0 h, 24 h, 48 h, and 72 h after energization. Then, the 3D volume data of the sample was compared with its initial 3D volume data before corrosion, taking the initial gray value distribution inside the sample before energization as the in-situ gray field, denoted as $f(x, y, z)$, and the gray value distribution after energization as the test gray field, denoted as $g(x, y, z)$. To calculate the volume strain and describe the transformation from the original position to the deformed position, where displacement is represented by a vector, the volume strain involves computing the displacement vector field by tracking gray value changes between the 3D images of the test group and the initial state.

Assume a point A inside the specimen moves to point A' after deformation. Due to the similarity in gray value distribution of point A and its adjacent area before and after deformation, the similarity degree of gray value distribution in a cube V with side length (2N+1) centered at A and A' can be quantified by establishing the functional relationship in equation (5). The increase in the function value is positively correlated with the similarity degree, i.e., the larger the function value, the higher the similarity between the two objects. By introducing different 3D coordinates (x, y, z) to solve the function value C(x, y, z) and finding the coordinate (x, y, z) that maximizes the function value, the deformed position of point A can be determined, and its displacement can be calculated. Using this method, multiple points are selected at predetermined intervals for calculation, and the displacements of all points are comprehensively analyzed to obtain the displacement values of each point in the specimen. Based on this, the displacement field within the specimen can be further calculated using gray field interpolation and correlation function values, and the first derivative of the anisotropy of the displacement field can be obtained to derive the strain field.

$$C(x, y, z) = \frac{\sum_{n=-N}^N \sum_{n=-N}^N \sum_{n=-N}^N (f(x_A + n, y_A + n, z_A + n) - \bar{f})(g(x + n, y + n, z + n) - \bar{g})}{\sqrt{\sum_{n=-N}^N \sum_{n=-N}^N \sum_{n=-N}^N (f(x_A + n, y_A + n, z_A + n) - \bar{f})^2} \sqrt{\sum_{n=-N}^N \sum_{n=-N}^N \sum_{n=-N}^N (g(x + n, y + n, z + n) - \bar{g})^2}} \quad (4)$$

where \bar{f} and \bar{g} represent the average gray values within the calculation sub-region, and (x_A, y_A, z) denote the coordinates of point A before deformation.

3. Compressive Strength Test Results Analysis

3.1. Surface Morphology Characteristics of Specimens

Figure 1 illustrates the surface morphology of specimens after immersion corrosion and electrochemical accelerated corrosion treatments. As the corrosive medium continuously penetrates, steel fibers undergo continuous corrosion, inevitably generating and propagating micro-cracks in the specimens [3]. It can be observed that the surface morphology of specimens immersed in 3.5% NaCl solution showed no significant changes, whereas those subjected to electrochemical accelerated corrosion exhibited varying degrees of rusting characteristics. Taking the surface morphology of specimens with 1.0% steel fiber volume fraction as an example, after current-induced corrosion, the damage on the anode surface was much more severe than that on the cathode surface. Specimens after 24 h of energization showed extensive rust seepage on the surface, almost covering the entire anode surface; after 48 h of energization, cracking initiated from the corners of the anode surface; after 72 h of energization, the number of cracks on the cathode surface increased, accompanied by rust seepage. This indicates that the presence of stray current significantly exacerbates corrosion damage, and its negative impact on structural durability must be highly emphasized.

Comparing the morphology of specimens with different steel fiber volume fractions after accelerated corrosion by energization, the degree of corrosion increased notably with the increase in steel fiber volume fraction. When the steel fiber volume fraction was 0.5%, the specimens showed minimal rust seepage and no obvious surface cracks; however, when the volume fraction was 1.5%, the specimens exhibited significant rust seepage on the surface, with visible cracks on the anode surface and even matrix spalling at the corners.

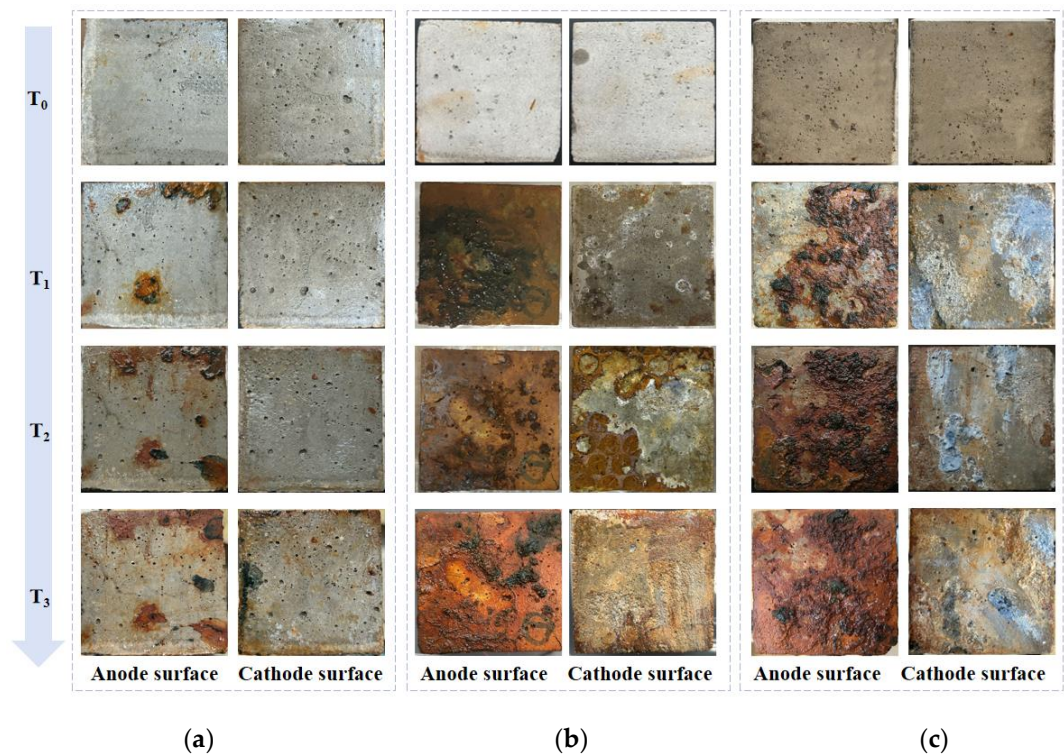


Figure 1. Surface morphology of specimens with different steel fiber volume contents after different electrification time (a) fiber volume content of 0.5%; (b) fiber volume content of 1.0%; (c) fiber volume content of 1.5%.

3.2. Compressive Strength Results

Figure 2 depicts the relationships among the compressive strength f_c , strength loss rate K_c , and steel fiber volume fraction of the material after different durations of stray current energization.

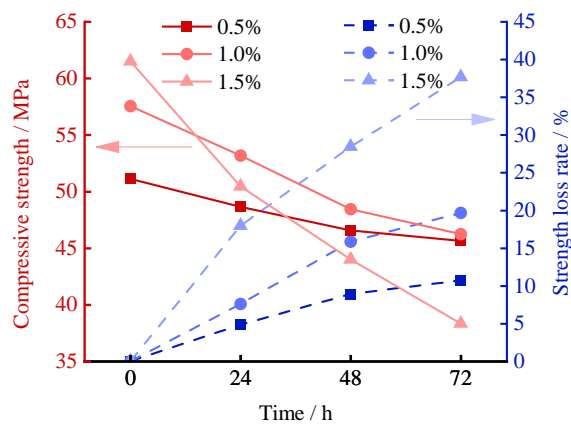


Figure 2. The changes of compressive strength and strength loss rate of the specimens.

As shown in Figure 2, both the compressive strength f_c and strength loss rate K_c exhibit a positive correlation with the steel fiber volume fraction, meaning that the compressive strength increases while the strength loss rate significantly rises with the increase in steel fiber content. The test results indicate that under the synergistic action of chloride ions and stray current, the mechanical properties of the material show a remarkable degradation trend. When the steel fiber volume fraction is 0.5%, the strength loss rates are 4.87%, 8.92%, and 10.73% with increasing corrosion degree, respectively. Notably, the compressive strength after 72 hours of stray current energization still exceeds that of the specimen without steel fibers, demonstrating the beneficial improvement of steel

fibers on the matrix. However, when the steel fiber volume fraction increases to 1.0% and 1.5%, the compressive strength loss becomes much more severe, with K_c values of 7.59%, 15.84%, 19.66% and 17.98%, 28.46%, 37.67%, respectively. This is because stray current enhances the permeability of chloride ions, and cracks in the matrix accelerate chloride ion penetration [7], jointly exacerbating the corrosion rate. The volume expansion of steel fiber corrosion products generates significant expansive stress in the matrix. When this rust-induced stress exceeds the crack resistance capacity of the fibers, it triggers matrix cracking and promotes crack propagation (Figure 1), leading to significant degradation of the material's macroscopic mechanical properties.

Figure 2 also reveals that a higher steel fiber volume fraction leads to more severe compressive strength loss. After 48 hours of energization, the compressive strength of T2-0.5% surpasses that of T2-1.5%. This is because a higher steel fiber content facilitates fiber connectivity, increasing the induced current [8] and accelerating corrosion. Excessive steel fibers also reduce matrix compactness, weakening its resistance to chloride ion invasion. When the volume expansion effect of steel fiber corrosion products exceeds their crack resistance, matrix cracks initiate and propagate. Under the combined action of stray current and cracks, the chloride ion migration rate significantly increases, accelerating steel fiber corrosion. This vicious cycle ultimately exacerbates material corrosion and mechanical property degradation.

3.3. Specimen Failure Morphology

Figure 3 illustrates the surface morphology characteristics of specimens after compressive failure. It is evident that the degree of specimen damage progressively intensifies with prolonged energization time. Specimens not subjected to the combined action of stray current and chloride ions exhibited no extensive matrix spalling, only developing multiple fine cracks; in contrast, specimens after 72 hours of energization showed pronounced through-thickness cracking and massive matrix spalling. This discrepancy arises because intensified corrosion of steel fibers—particularly for those near the surface—causes severe cross-sectional degradation, drastically impairing their crack-arresting capacity. The formation of corrosion products induces intra-specimen micro-cracking, ultimately leading to surface spalling and marked compressive strength degradation.

Furthermore, for non-energized specimens, increasing steel fiber volume fraction progressively mitigates crack propagation. However, under corrosive conditions, an inverse trend emerges: 1.5% steel fiber specimens exhibited significantly greater post-failure damage than 0.5% counterparts. This aligns with compressive strength findings, where 1.5% specimens suffered more severe corrosion-induced fiber degradation, diminishing their reinforcing efficiency. Consequently, they failed to restrict crack growth, exacerbating global deterioration. This indicates that while high fiber content enhances initial crack resistance, cumulative corrosion-induced damage substantially reduces load-bearing capacity. Mechanistically, elevated fiber density enhances inter-fiber conductivity, promoting local corrosion cell formation under stray current-chloride coupling, which accelerates corrosion. Additionally, corrosion product expansion triggers matrix cracking, propagating fractures and compromising structural integrity.

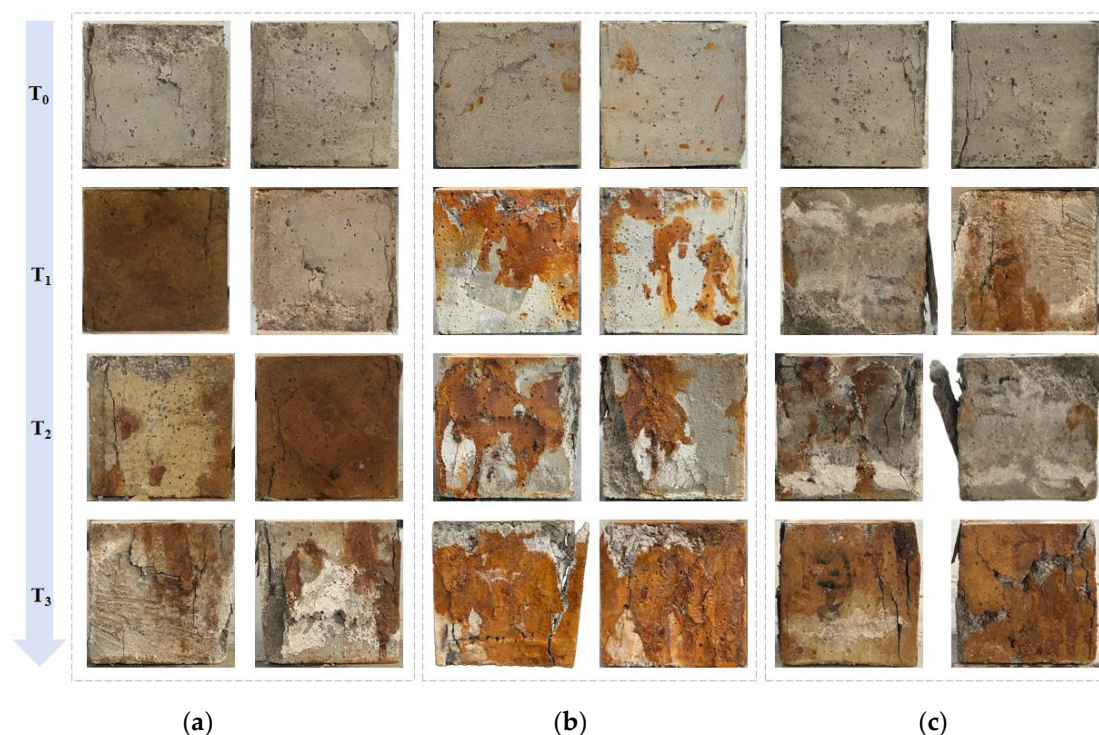


Figure 3. Surface morphology of damaged specimens with different steel fiber contents under different electrification time (a) fiber volume content of 0.5%; (b) fiber volume content of 1.0%; (c) fiber volume content of 1.5%.

4. CT Test Results

4.1. CT Image Analysis

Due to the minimal corrosion degree of 0.5% volume fraction specimens, 2D grayscale images of the same-height cross-sections from 1.0% and 1.5% specimens at different energization times were selected, specifically sections with obvious cover layer damage for evaluating corrosion damage processes, as shown in Figure 4.

For the 1.0% specimens, cross-sectional images at T_0 and T_1 show no significant differences, indicating that steel fibers' good corrosion resistance mitigates stray current damage during the initial stage [9]. However, T_2 and T_3 images reveal corrosion products filling adjacent pores and multiple micro-cracks in the matrix, likely caused by internal expansive stress from continuous rust accumulation. The 1.5% specimens exhibit more severe corrosion, with obvious pore filling by rust products and even visible matrix spalling at the lower-right corner, where micro-cracks emerge as early as T_2 .

Analysis of cross-sectional morphology shows distinct spatial distribution of crack initiation and propagation: Initial cracks predominantly originate from corner regions and then extend toward the center. Notably, steel fibers around larger cracks exhibit significantly reduced gray values, indicating severe corrosion where fibers are enveloped by rust products.

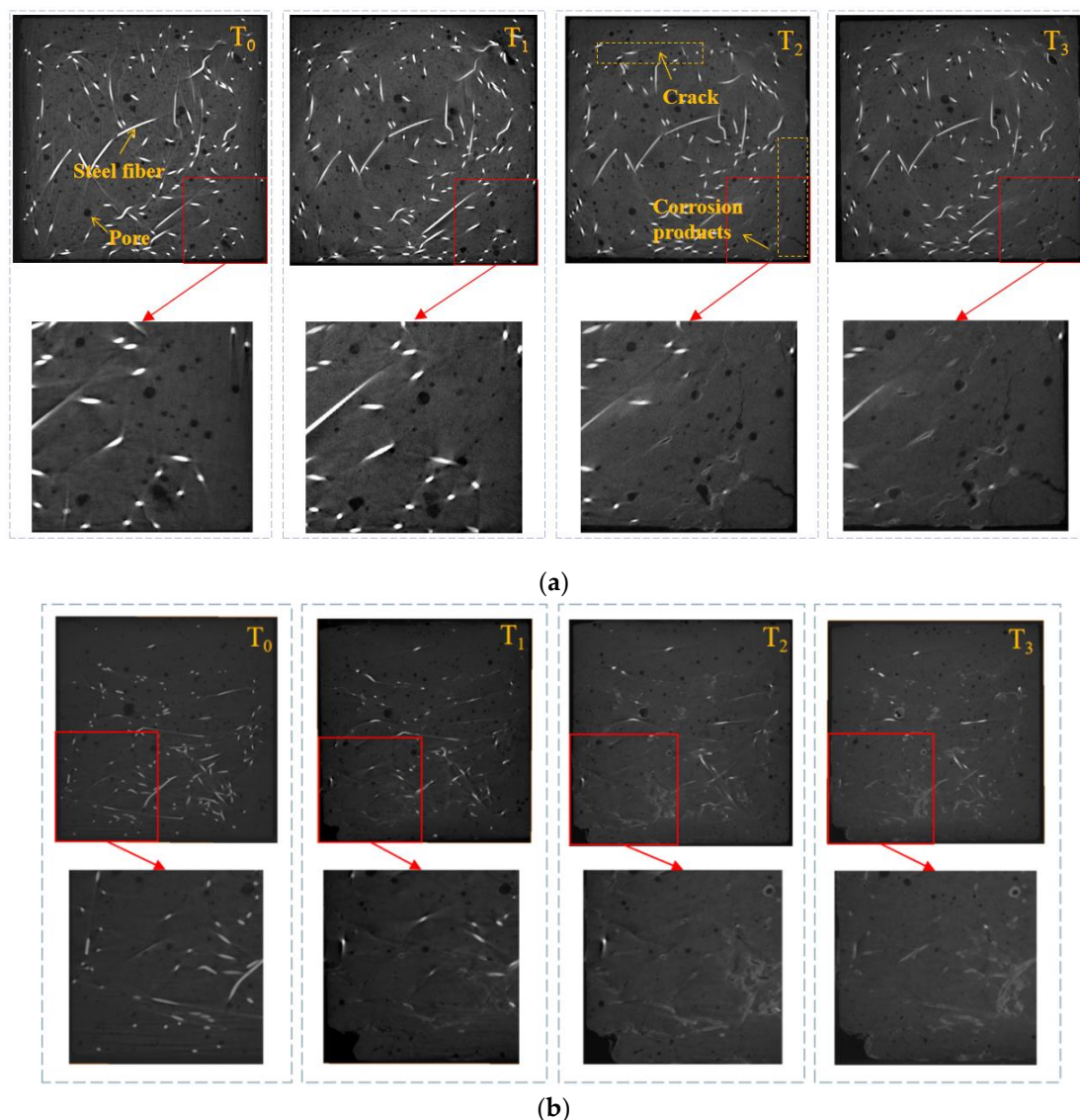


Figure 4. Cross-sectional images at the same height level for specimens with different fiber volume fractions subjected to various electrification durations (a) fiber volume content of 1.0%; (b) fiber volume content of 1.5%.

4.2. Quantitative Analysis of CT Images

4.2.1. Analysis of Steel Fiber Volume Loss

In specimens with 1.0% steel fiber content, the free space for fiber flow is significantly reduced due to the higher fiber content. For 1.5% volume fraction specimens, the non-uniform distribution of steel fibers becomes more pronounced, as increased fiber content deteriorates the workability of steel fiber-reinforced concrete [10]. High fiber dosages tend to cause fiber clustering, a non-uniform state that affects the material's mechanical properties and isotropy.

Taking 1.0% steel fiber specimens as an example, 3D reconstruction images (Figure 5) show that the matrix at T₁ exhibits only partial rust seepage without obvious damage. However, starting from T₂, cracks first appear at the lower-right corner of the matrix and gradually propagate inward. For the steel fiber phase, little volume change is observed between T₀ and T₁, but from T₂ onward, steel fibers near the surface suffer severe volume loss, with matrix cracks preferentially emerging in high-fiber-content regions. This is because steel fibers inevitably located near the specimen surface have a negligible cover layer thickness, making them susceptible to corrosion under combined stray current and chloride ion action. Thus, extensive rust seepage on the specimen surface indicates severe steel

fiber corrosion—millimeters-deep corrosion occurs in surface-proximal fibers under chloride attack, while inner fibers remain relatively intact [11].

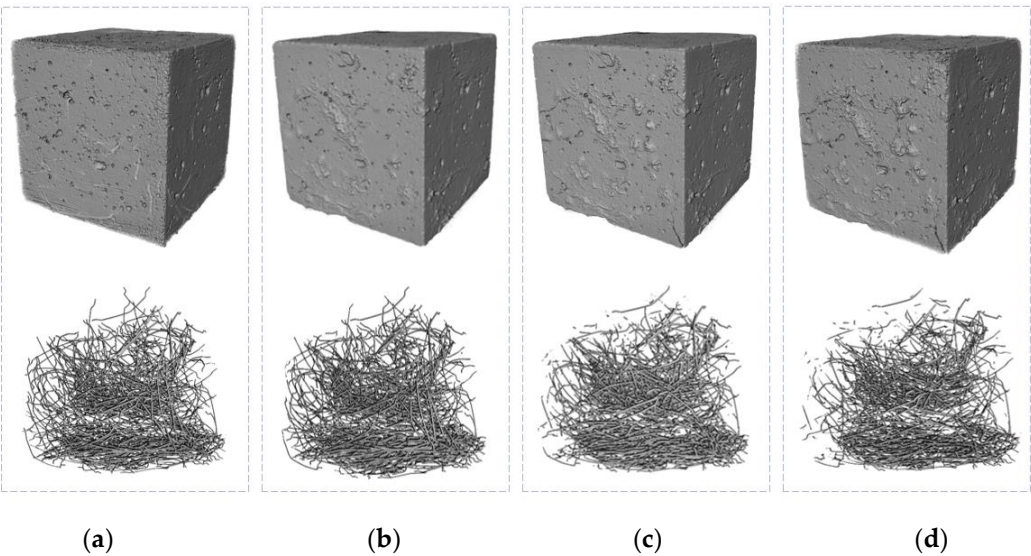


Figure 5. 3D reconstruction images of specimens with a content of 1.0% under different power duration (a) T₀; (b) T₁; (c) T₂; (d) T₃.

By extracting steel fibers, their volumes were quantitatively calculated as shown in Table 3. For 1.0% volume fraction specimens, the steel fiber volume loss rates from T₁ to T₃ were 1.72%, 9.48%, and 15.98%, respectively, with growth rates of 1.72%, 7.76%, and 6.50%. Results show that steel fiber volume decreases progressively with extended energization, attributed to corrosion-induced volume loss. Corrosion products, with densities lower than steel, occupy 2 to 6 times the original material volume [12]. This volumetric expansion triggers cover layer cracking, creating rapid pathways for aggressive media (e.g., moisture and chloride ions), thus accelerating corrosion in cracked regions. Consequently, the volume loss rate growth at T₂ is notably higher than that at T₁. Quantitative analysis of steel fiber volume changes enables accurate evaluation of fiber corrosion degree.

Table 3. Volume and volume loss rate of steel fiber with different dosage at different time.

Fiber dosage / %	Parameters	T ₀	T ₁	T ₂	T ₃
0.5	Volume / mm ³	3641.87	3575.22	3523.15	3433.92
	Volume loss rate / %	0	1.83	3.26	5.71
1.0	Volume / mm ³	7129.93	6864.70	6453.46	5990.57
	Volume loss rate / %	0	3.72	9.48	15.98
1.5	Volume / mm ³	10674.65	9507.91	8247.23	7423.15
	Volume loss rate / %	0	10.93	22.74	30.46

4.2.2. Pore Structure Analysis

The presence of pores in the matrix not only affects the transport of harmful media like chloride ions but also directly influences the distribution of corrosion products, rust-induced stress, and the

entire process of rust expansion cracking. Therefore, to further investigate the corrosion damage mechanism of steel fiber-reinforced concrete, studying the pore size distribution and spatial distribution in specimens is crucial, requiring analysis of the 3D pore structure of specimens with different steel fiber dosages. Based on CT results, pores were visually characterized by color coding: pores with diameters less than 1000 μm are shown in blue, while those larger than 1000 μm are in red, as depicted in Figure 6. The figure reveals that with the increase in steel fiber content, both the number of red pores and blue pores increases, exhibiting a more dense distribution.

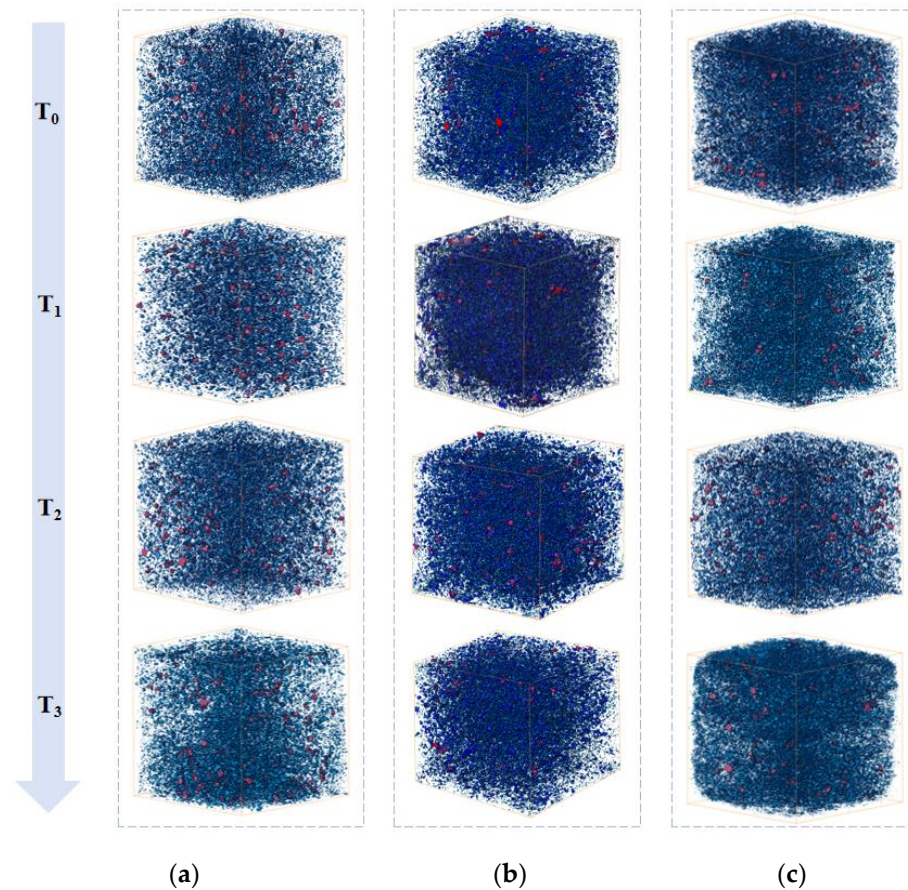


Figure 6. Three-dimensional pore structure diagram of each steel fiber volume at different time (a) fiber volume content of 0.5%; (b) fiber volume content of 1.0%; (c) fiber volume content of 1.5%.

To comprehensively analyze and evaluate the pore structure, quantitative calculations were performed on the pore size distribution ratios of specimens with different steel fiber dosages after varying energization times, as listed in Table 4. Extracted pores were classified into seven size intervals: <0.11 mm, 0.11–0.25 mm, 0.25–0.35 mm, 0.35–0.50 mm, 0.50–0.75 mm, 0.75–1.00 mm, and >1.00 mm [13], to observe proportional changes with deepened corrosion. Comparison of Table 4 reveals similar pore size distribution patterns across the three steel fiber volume fractions, but porosity exhibits an increasing trend with higher fiber content, accompanied by a significant rise in the volume fraction of pores larger than 500 μm . For 0.5%, 1.0%, and 1.5% steel fiber specimens, the volume fractions of pores >500 μm are 7.62%, 13.15%, and 16.40%, respectively. The increased proportion of large pores deteriorates the pore structure and reduces matrix density. This stems from heightened probability of steel fiber agglomeration with higher dosages—particularly for 1.5% specimens, which promotes formation of large pores and internal defects—the large specific surface area of steel fibers [14] introducing excessive air during mixing, and increased fiber connectivity probability reducing matrix density [15], thus facilitating penetration of external moisture and ions. Consequently, 1.0% and 1.5% specimens suffer more severe corrosion damage than 0.5% counterparts during energization.

Table 4. Proportion of pore size for specimens (%).

No.	Range of diameter /mm						
		<0.11	0.11-0.25	0.25-0.35	0.35-0.5	0.5-0.75	0.75-1 >1
T0-0.5%		40.35	32.16	11.92	7.95	4.83	1.64 1.15
T1-0.5%		42.26	30.18	10.61	8.04	4.37	2.05 1.49
T2-0.5%		43.11	29.12	12.18	7.94	4.81	1.57 1.27
T3-0.5%		44.20	28.65	12.47	7.73	4.42	1.47 1.07
T0-1.0%		36.25	28.42	12.21	9.97	7.63	2.87 2.65
T1-1.0%		38.71	27.06	13.69	8.10	6.72	3.69 2.03
T2-1.0%		40.86	27.98	12.37	8.42	7.32	1.21 1.84
T3-1.0%		42.33	30.17	11.4	7.46	5.43	1.49 1.72
T0-1.5%		34.59	22.38	14.21	12.43	9.43	3.77 3.20
T1-1.5%		38.99	21.91	13.77	11.32	8.21	3.18 2.62
T2-1.5%		39.35	25.21	12.99	10.27	7.13	2.79 2.25
T3-1.5%		40.24	25.1	12.89	10.07	6.92	2.67 2.13

Additionally, prolonged energization leads to a continuous increase in the proportion of small pores (<0.11 mm) in the matrix. Taking 1.5% steel fiber specimens with the most severe corrosion as an example, small pores accounted for 40.35% in initial samples, increasing to 44.20% after 72 hours of energization—these small pores are less susceptible to damage during processing [15]. Meanwhile, the proportion of large pores gradually decreases, as corrosion products from steel fiber rust preferentially fill pores, with similar growth rates across all pore size ranges maintaining relative proportional constancy. Notably, despite the increase in small pores, the overall matrix strength is not significantly improved. Instead, volume expansion of corrosion products induces internal stress accumulation, causing micro-cracking within the matrix, particularly evident at the steel fiber-matrix interface. These micro-cracks may provide pathways for crack propagation at later stages, accelerating concrete degradation.

The growth rate of small pores is rapid within the first 24 hours of energization but plateaus between 24 and 72 hours. This indicates that corrosion products quickly fill existing pores in the early corrosion stage, while in later stages, with pores gradually saturated, corrosion products primarily exert pressure on the matrix, inducing new micro-crack generation rather than further increasing pore proportion. In summary, the increase in small pores and decrease in large pores during accelerated corrosion by energization directly reflect the filling effect of corrosion products, but this process is accompanied by the generation and propagation of interfacial micro-cracks, compromising the long-term durability of concrete. These findings further reveal the complex influence of steel fiber corrosion on matrix pore structure evolution.

4.3. DVC Analysis Results

4.3.1. Displacement Field

The displacement field reasonably reflects the matrix deformation behavior under different conditions, enabling the understanding of crack development trends. Displacement fields were obtained via software processing for 1.0% steel fiber specimens after 24 h, 48 h, and 72 h of accelerated corrosion by energization, compared with their initial states. The results are visualized by color-coded displacement amplitudes, as shown in Figure 7.

With the increase in corrosion degree, the displacement amplitude significantly increases, and regions with large displacements typically appear at the corners of the specimen. This indicates that the material can more effectively redistribute loads when stressed [16], meaning that the addition of fibers allows external forces to disperse uniformly throughout the specimen rather than concentrate in local areas—thus resulting in the maximum displacement at the corners. This causes the specimen to tend toward ductile failure, and the load redistribution mechanism significantly enhances the material's overall performance, improving its reliability in practical engineering applications.

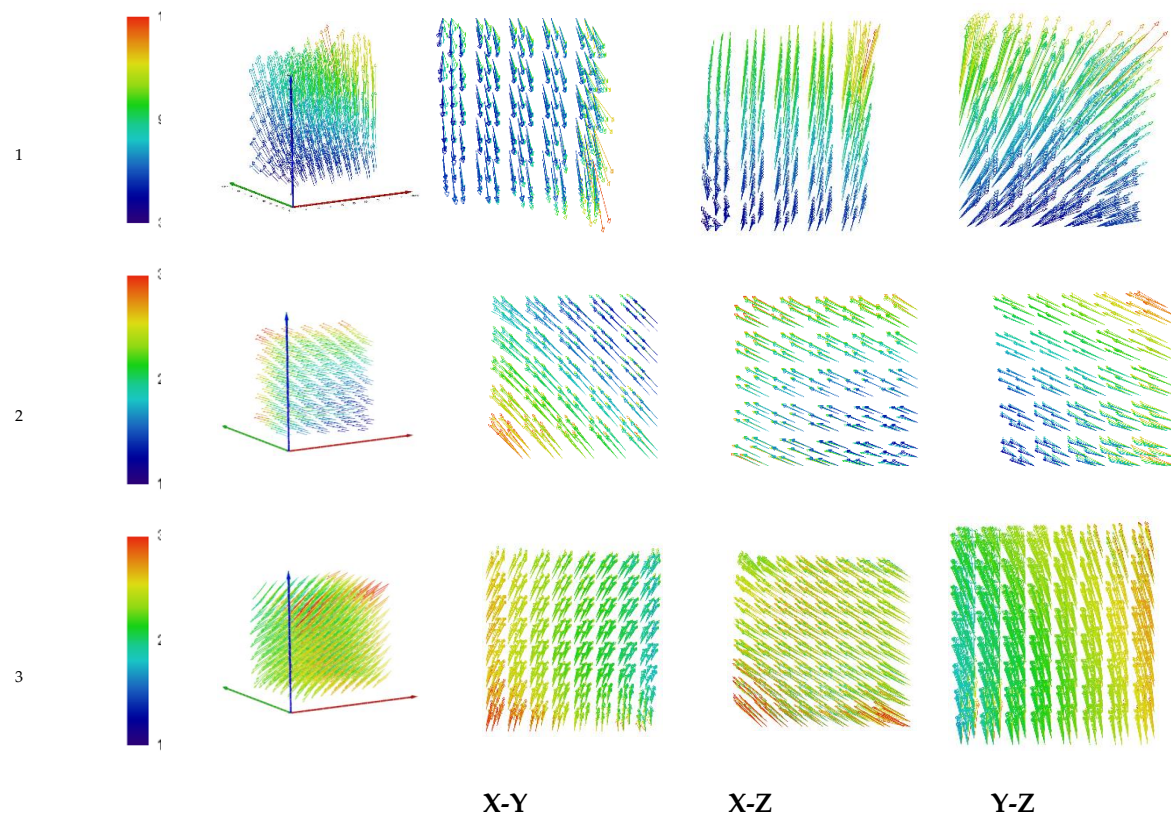


Figure 7. Displacement field of the specimen with fiber volume content of 1.0%.

4.3.2. Strain Field

Figure 8 presents the strain field calculation results. It is observed that matrix displacement increases with the degree of corrosion, and stress concentration preferentially occurs at edges with pore damage or in regions with sparse internal fibers. As shown in Figure 8c, in fiber-dense zones, fibers bridge cracks, disperse stress, and prevent crack coalescence, forming a fine and dispersed crack network that allows the specimen to maintain residual compressive strength. Conversely, regions with fewer fibers exhibit higher brittleness due to stress concentration, promoting crack propagation, highlighting the role of fibers in resisting deformation and inhibiting crack growth. The elastic modulus mismatch between steel fibers and concrete induces local stress concentration at the

fiber-matrix interface, but fibers significantly enhance the material's overall structural performance by altering crack propagation paths and mitigating sudden failure [16].

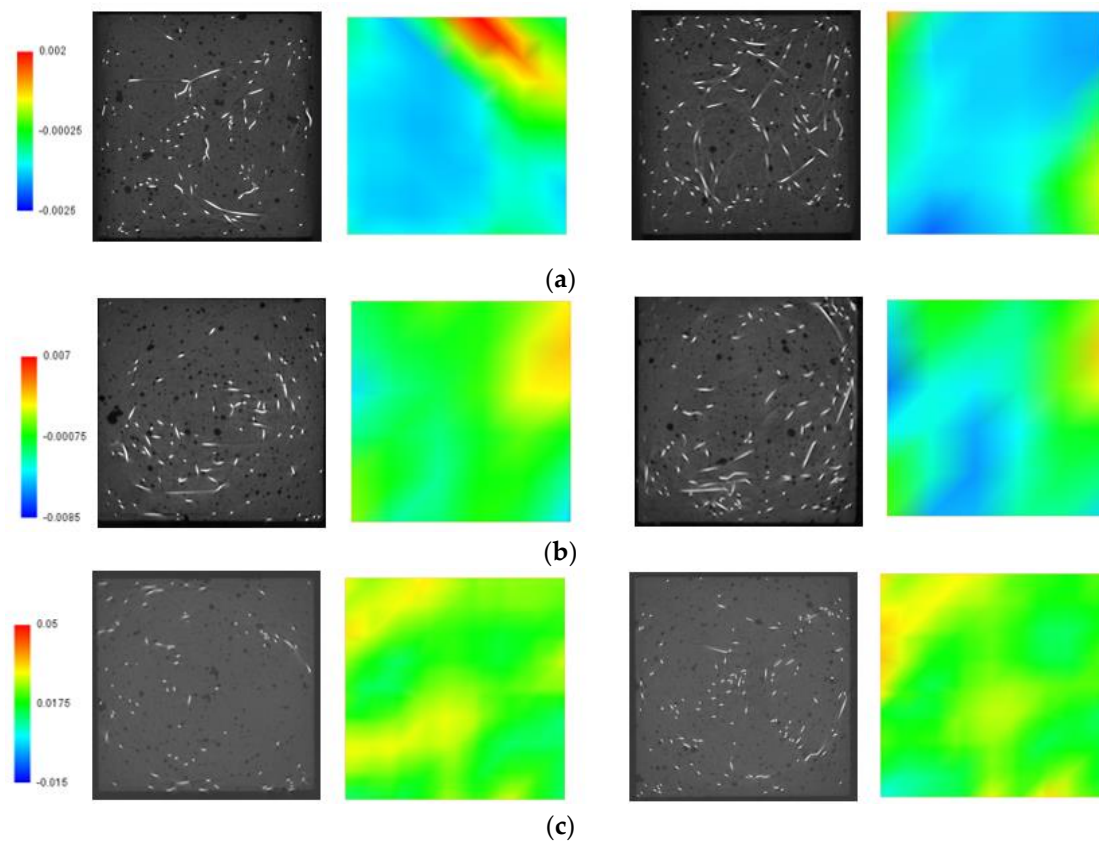


Figure 8. Strain field of the specimen with fiber content of 1.0%.

5. Conclusions

This paper investigates the effects of energization time and steel fiber volume fraction on the compressive strength of specimens through accelerated corrosion tests simulating stray current, and monitors the corrosion process of steel fiber-reinforced concrete via X-CT, including in-situ observation of steel fiber corrosion product accumulation and matrix rust expansion cracking, to analyze the corrosion mechanism at the microscale. The main conclusions are as follows:

(1) The corrosion degree of steel fibers and their volume fraction significantly affect the compressive strength of specimens. When steel fibers are non-corroded, the compressive strength of 1.5% steel fiber specimens is notably higher than that of 0.5% specimens. However, with deepened corrosion, severe steel fiber volume loss causes the compressive strength of 0.5% specimens to surpass that of 1.5% specimens after 48 hours of energization. The 1.5% specimens exhibit severe strength degradation, with a strength loss rate K_c as high as 37.67% after 72 hours of energization, compared to only 10.73% for 0.5% specimens.

(2) Quantitative analysis of CT images (steel fiber volume loss rate, pore distribution) reveals that during the initial corrosion stage, steel fiber corrosion products first fill pores, then exert pressure on the surrounding matrix, inducing micro-cracking and structural degradation. Specimens with 0.5% steel fiber content show low corrosion degree, minimal volume loss, and the highest proportion of small pores (<0.11 mm), resulting in dense matrix. In contrast, 1.5% specimens suffer severe corrosion due to fiber clustering during mixing, which increases the proportion of large pores (>1 mm). Steel fiber volume loss in 1.5% specimens increases drastically from 48 hours onward.

(3) Displacement and strain field results from DVC show that steel fibers enable uniform load distribution throughout the specimen, with maximum displacement at corners reducing stress concentration. Stress concentration preferentially occurs at edges with pore damage or in fiber-sparse

regions. Fibers bridge cracks, disperse stress, and prevent crack coalescence, highlighting their role in resisting deformation and inhibiting crack propagation.

Author Contributions: Conceptualization, Y. Z. (Yurong ZHANG) and Z.C.; methodology, Z.Y.; validation, L.Y., B.L. and M.L.; formal analysis, M.L.; data curation, B.L.; writing—original draft preparation, Z.Y.; writing—review and editing, Y. Z.; project administration, Y. Z.; funding acquisition, Y. Z. All authors have read and agreed to the published version of the manuscript.

Funding: This research was funded by National Natural Science Foundation of China, grant number 52408303.

Conflicts of Interest: The authors declare no conflicts of interest.

References

- DENG Y G, LI Y. Evaluating the chemical stability and performance of zinc phosphate-coated steel fibers in concrete corrosion simulations [J]. *Materials Today Communications*, 2024, 41: 110363.
 - SHEN J, PAN Q. The improving effect of steel fiber on crack resistance of ultra-deep buried concrete shield tunnels [J]. *Building Structure*, 2023, 53 (S2): 2721-2724.
 - BERROCAL C G, LUNDGREN K, LÖFGREN I. Corrosion of steel bars embedded in fibre reinforced concrete under chloride attack: State of the art [J]. *Cement and Concrete Research*, 2016, 80: 69-85.
 - LIN L B, LAI X Y, FENG Z W. Experimental study on the strength of steel fiber reinforced concrete under the combined effect of stray current and chloride ion corrosion [J]. *Journal of Xiamen University(Natural Science)*, 2018, 57(03): 425-431.
 - ZHAO J, LI H J, GAO D Y. Mechanical performances of steel fiber and steel fiber reinforced concrete after corrosion [J]. *Journal of Building Materials*, 2015, 18(03): 409-414.
 - WANG P, QIAO H, ZHANG Y, et al. Three-dimensional characteristics of steel corrosion and corrosion-induced cracks in magnesium oxychloride cement concrete monitored by X-ray computed tomography [J]. *Construction and Building Materials*, 2020, 246: 118504.
 - MANGAT P S, GURUSAMY K. Corrosion resistance of steel fibres in concrete under marine exposure [J]. *Cement and Concrete Research*, 1988, 18(1): 44-54.
 - WANG C C, DU H X, SHI L N, et al. Experimental study on electrical properties of carbon fiber-steel fiber cement matrix composites [J]. *Bulletin of the Chinese Ceramic Society*, 2022, 41(08): 2696-2705.
 - JANG Y S, OH T, BANTHIA N, et al. Effects of nano-SiO₂ coating and induced corrosion of steel fiber on the interfacial bond and tensile properties of ultra-high-performance concrete (UHPC) [J]. *Journal of Building Engineering*, 2022, 54: 104637.
 - YANG J, CHEN B, NUTI C. Influence of steel fiber on compressive properties of ultra-high performance fiber-reinforced concrete [J]. *Construction and Building Materials*, 2021, 302: 124104.
 - WANG T, ZHAO J J, YANG Y X. Effect of steel fiber and carbon nanotube on resistance of ultra-high performance concrete to chloride ion penetration [J]. *Building Structure*, 2024, 54(01): 128-132+118.
 - XU G, BAO H, WANG Q, et al. Research on volumetric expansion ratio of corrosion products in concrete structure [J]. *Journal of Huazhong University of Science and Technology(Natural Science Edition)*, 2015, 43(09): 105-109.
 - TAHERI-SHAKIB J, AL-MAYAH A. 4D evolutions of cracks, voids, and corrosion products in reinforced concrete materials [J]. *Nature Scientific Reports* 13, 2023, 22455.
 - ZHOU X B, JIANG Z H, ZHANG W W, et al. Experimental study on cement mortar reinforced by amorphous alloy fiber [J]. *Journal of Changjiang River Scientific Research Institute*, 2017, 34(05): 120-124.
 - RUI Y, KANGNING L, TIANYI Y, et al. Comparative study on the effect of steel and polyoxymethylene fibers on the characteristics of Ultra-High Performance Concrete (UHPC) [J]. *Cement and Concrete Composites*, 2022, 127: 104418.
 - WANG C, DU Z, ZHANG Y, et al. Meso-structural insights into post-peak behaviors of micro steel fiber-reinforced recycled aggregate concrete using in-situ 4D CT and DVC techniques [J]. *Journal of Building Engineering*, 2025, 100: 111674.
- Author 1, A.B.; Author 2, C.D. Title of the article. *Abbreviated Journal Name* Year, Volume, page range.

Disclaimer/Publisher's Note: The statements, opinions and data contained in all publications are solely those of the individual author(s) and contributor(s) and not of MDPI and/or the editor(s). MDPI and/or the editor(s) disclaim responsibility for any injury to people or property resulting from any ideas, methods, instructions or products referred to in the content.